# A Next-Generation Hard X-Ray Nanoprobe Beamline for *In Situ* Studies of Energy Materials and Devices

JÖRG MASER, BARRY LAI, TONIO BUONASSISI, ZHONGHOU CAI, SI CHEN, LYDIA FINNEY, SOPHIE-CHARLOTTE GLEBER, CHRIS JACOBSEN, CURT PREISSNER, CHRIS ROEHRIG, VOLKER ROSE, DEMING SHU, DAVID VINE, and STEFAN VOGT

The Advanced Photon Source is developing a suite of new X-ray beamlines to study materials and devices across many length scales and under real conditions. One of the flagship beamlines of the APS upgrade is the *In Situ* Nanoprobe (ISN) beamline, which will provide *in situ* and *operando* characterization of advanced energy materials and devices under varying temperatures, gas ambients, and applied fields, at previously unavailable spatial resolution and throughput. Examples of materials systems include inorganic and organic photovoltaic systems, advanced battery systems, fuel cell components, nanoelectronic devices, advanced building materials and other scientifically and technologically relevant systems. To characterize these systems at very high spatial resolution and trace sensitivity, the ISN will use both nanofocusing mirrors and diffractive optics to achieve spots sizes as small as 20 nm. Nanofocusing mirrors in Kirkpatrick–Baez geometry will provide several orders of magnitude increase in photon flux at a spatial resolution of 50 nm. Diffractive optics such as zone plates and/or multilayer Laue lenses will provide a highest spatial resolution of 20 nm. Coherent diffraction methods will be used to study even small specimen features with sub-10 nm relevant length scale. A high-throughput data acquisition system will be employed to significantly increase operations efficiency and usability of the instrument. The ISN will provide full spectroscopy capabilities to study the chemical state of most materials in the periodic table, and enable X-ray fluorescence tomography. *In situ* electrical characterization will enable *operando* studies of energy and electronicdevices such as photovoltaic systems and batteries. We describe the optical concept for the ISN beamline, the technical design, and the approach for enabling a broad variety of *in situ* studies. We furthermore discuss the application of hard X-ray microscopy to study defects in multi-crystalline solar cells, one of the lines of inquiries for which the ISN is being developed.

DOI: 10.1007/s11661-013-1901-x


## I. INTRODUCTION

THE development of hard X-ray nanoprobes with a spatial resolution of below 100 nm has enabled the study of a new generation of complex systems, such advanced materials and materials systems, nanoscale devices, and biologic cells, and tissues.[1–7] Hard X-ray nanoprobes utilize X-ray fluorescence, diffraction, and coherent techniques in both transmission and Bragg geometries to study composition, structure, and strain in 2D and 3D samples with a thickness of many micrometers, and with sensitivity to trace amounts of material and thin layers and interfaces. While these advances have opened a new window into nanoscale phenomena, most high-resolution studies performed to date are done *ex situ*, and at or near room temperature.

The *In Situ* Nanoprobe beamline (ISN beamline) is aimed at the *in situ* and *operando* study of materials and materials systems, including advanced energy harvesting,[8–12] energy conversion[13–15] and energy storage systems,[16–18] and nanoelectronics.[19–23] Examples of such systems include organic and inorganic solar cells, fuel cell components, and concepts for advanced batteries. Studies on nanoelectronics will include the study of complementary metal-oxide semiconductor (CMOS) devices designed for 22-nm node technologies and below, with a view to increased performance, speed, and power efficiency. The ISN will furthermore study processes and approaches aimed at sustainable construction and carbon capture, such as environmentally benign building materials, understanding of natural carbon sinks, and development of artificial carbon sinks.[24–30] All these systems have in common complex, hierarchical structures with nanoscale features, often in nonplanar geometries, where small quantities of inhomogeneously distributed dopants, precipitates, contaminants, and second-phase particles play an increasingly important role in overall system performance. In most

JÖRG MASER, BARRY LAI, ZHONGHOU CAI, LYDIA FINNEY, SOPHIE-CHARLOTTE GLEBER, DAVID VINE, Physicists, SI CHEN, Postdoctoral Research Assistant, CHRIS JACOBSEN, Associate Division Director, CURT PREISSNER, Engineer, CHRIS ROEHRIG, Scientific Associate, VOLKER ROSE, Assistant Physicist, DEMING SHU, Senior Engineer, and STEFAN VOGT, Physicist, Group Leader, are with the Advanced Photon Source, Argonne National Lab, Argonne, IL. Contact e-mail: maser@anl.gov TONIO BUONASSISI, Assistant Professor, is with the Massachusetts Institute of Technology, Cambridge, MA.
Manuscript submitted March 1, 2013.
Article published online August 20, 2013

cases, very high spatial resolution, and imaging at trace-level sensitivities in complex 2-D or 3-D geometries is required. To understand and control material properties that determine system performance, system efficiency, and environmental impact, characterization of these systems must be performed at low or elevated temperature, under reactive gases, at fixed partial pressures of relevant elemental and chemical system constituents, under applied external fields, or during operation and cycling.

**Table I. Working Distances for Nanofocusing Optics with Resolution Limits of 50 and 20 nm for a Distance of the ISN Instrument of 72 m from the X-ray Source**

| | Working Distance for ISN at 72 m From Source | |
|---|---|---|
| Spatial Resolution Limit | 50 nm | 20 nm |
| Nanofocusing Optic | focusing mirror | zone plate/MLL |
| Working Distance | 27 mm | 7.5 mm |

For diffraction optics, the working distance is calculated for a photon energy of 10 keV. For reflective optics, the working distance is independent of the photon energy.

## II. OPTICAL DESIGN OF *IN SITU* NANOPROBE BEAMLINE

The ISN beamline is aimed at highest-resolution imaging, spectroscopy, and tomography of energy materials and energy devices, as well as of other complex systems, as outlined above. The ISN beamline will provide a spot size of 20 nm using diffractive optics,[31–33] and of 50 nm using non-dispersive reflective optics.[34,35] The ISN instrument will provide variable temperature, flow of gases and fluids, and applied electric fields, toward the study of properties of materials and devices under *in situ* conditions, including materials fabrication and device operation. To perform resonant studies of technologically relevant elements, the ISN beamline will operate with hard X-rays with photon energies between 4 and 30 keV. The beamline optics are designed to provide adjustment of the lateral coherence length and the bandpass of the X-rays. The beamline uses mirror optics for beam steering, higher harmonics rejection, and power management, as well as crystal and multilayer monochromators to select photon energy and bandpass.

The ISN instrument will use elliptically figured mirror optics to focus X-rays with large bandpass to a spot size of 50 nm; it will use diffractive optics such as zone plates (ZPs) or multilayer Laue lenses (MLLs) to focus X-rays with small bandpass to a spatial resolution of 20 nm or below. Both reflective optics and MLL optics are capable of providing good focusing efficiency even at high photon energies, where the coherent flux is small. The ISN will integrate components designed to provide *in situ* environments: a heating/cooling stage to provide temperatures between 40 K (−233 °C) and 773 K (~500 °C), a high-temperature stage with adjustable temperature to provide temperatures of 1273 K (1000 °C) or above, sample cells that accommodate flow of gases and fluids, and cells optimized for application of electric fields. The ISN will be optimized for X-ray fluorescence detection. Toward that purpose, the design calls for simultaneous use of two fluorescence detectors with large solid-angle capability, with the goal of achieving a total solid-angle coverage approaching $\pi$ sr. Complementary to fluorescence detection, the ISN will provide phase contrast as well as coherent diffractive imaging capabilities. This will allow simultaneous mapping of low-Z matrices using hard X-rays, and provide, in ptychographic mode, an avenue toward super-resolution of below 10 nm.[36,37] To optimize characterization of hierarchically organized systems, the ISN will operate at different length scales, and allow efficient switching between a high-flux configuration that uses partially coherent X-rays with large bandwidth, and a high-resolution configuration that uses spatially coherent X-rays with a small bandpass. The ISN will furthermore deploy fly scanning techniques to allow acquisition of high-resolution maps with a large number of pixels in 2D and 3D.

The ISN beamline is designed as one of two independently operating branch beamlines at a canted insertion device front end, and is currently anticipated to be implemented as a new branch beamline at APS Sector 32, using the inboard and downstream part of the sector 32 floor. The ISN beamline is designed to maximize the coherent photon flux on the sample, by combining a beamline design based on a spatial filter with nanofocusing optics that match the lateral coherence length of X-rays.

To maximize the working distance of the focusing optics and accommodate various *in situ* sample cells, it is important that the lateral coherence length in the end station be as large as possible, which in turn requires positioning of the ISN as far as possible from the source, at 72 to 75 m. This corresponds to a focal length of 22 mm and a working distance of ~7.5 mm at photon energies between 6 and 30 keV, using diffractive optics with a spatial resolution limit of 20 nm. The working distance of reflective optics with a spatial resolution of 50 nm is 25 to 27 mm, limited by a scattering aperture at the downstream side of the nanofocusing mirror. Table I shows working distances for optics with resolution limits of 50 and 20 nm, for a distance of the ISN instrument at 72 m from the X-ray source. As spatial coherence criterion, we use the relation $d\theta = \lambda/2$, where $d$ is the FWHM source size, $\theta$ the FWHM full angle, and $\lambda$ the X-ray wavelength.

One of the primary tasks of the beamline layout is to define and propagate a spatially coherent wavefront from the insertion device to the nanofocusing optics. At the same time, the effect of positional and angular instabilities of beamline optics such as mirrors and monochromators on focal spot size and focal position must be minimized. These tasks are achieved by (i) positioning all beamline optics upstream of a beam-defining aperture (BDA) and (ii) enabling the BDA to close to a value $d$ sufficiently small to define a secondary, spatially coherent source (Figure 1). The BDA represents a secondary source, with stability defined only by

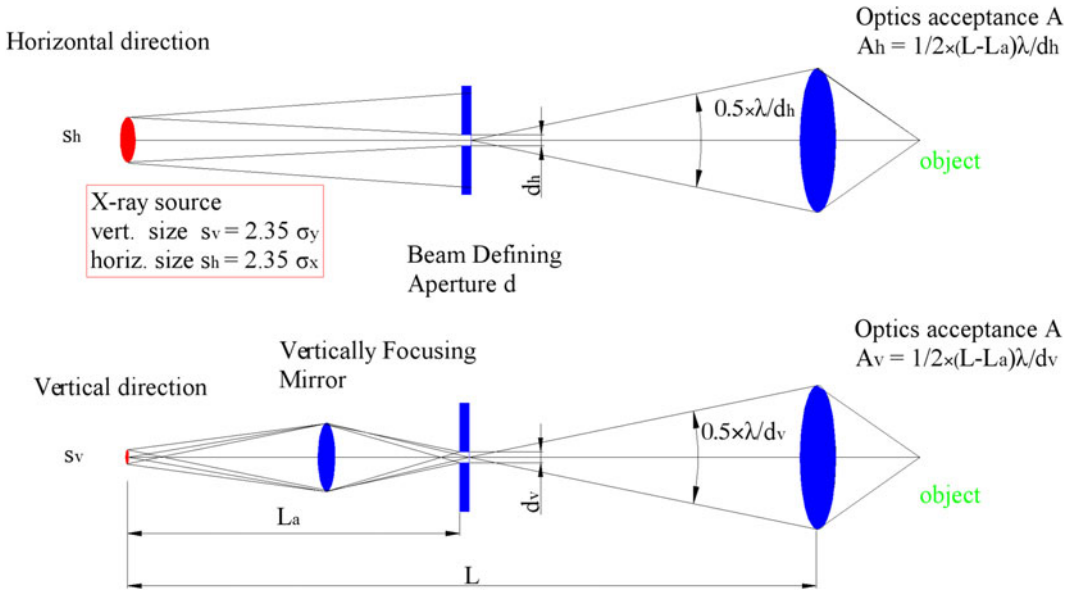


Fig. 1—Optical layout of the ISN beamline. $\sigma_h$ and $\sigma_v$ are the FWHM horizontal and vertical source sizes, respectively, $\sigma_h = 2.35\ \sigma_x$, and $\sigma_v = 2.35\ \sigma_y$. L is the distance of the nanofocusing optics from the source, $L_a$ is the distance of the beam defining aperture from the source, and $d_h$ and $d_v$ the size of the BDA in horizontal and vertical direction. $A_h$ and $A_v$ are the acceptance of the nanofocusing optics in horizontal and vertical direction, where the acceptance corresponds to the aperture $D$ of a diffractive optic, or to the product of grazing angle and optical length for a nanofocusing mirror. The beam defining aperture can be set to horizontal/vertical size $d_h$ and $d_v$ which allows fully or partially coherent illumination of the different apertures of both reflective and diffractive nanofocusing optics.

its mechanical and optical properties. Any imperfections, vibrations or drifts by the beamline optics will therefore be filtered out by the BDA, and materialize at the sample position as intensity change, but not as (virtual) motion of the source. By positioning all beamline optics upstream of the BDA, the BDA will be illuminated only by monochromatic X-rays, thereby minimizing the power it is exposed to, and maximizing the accuracy of its position and size. In the horizontal direction, the BDA can be closed to a size of as small as 10 $\mu$m, to provide coherent illumination of both diffractive and reflective X-ray optics in the horizontal direction. In the vertical direction, a pink-beam mirror M2 is used to refocus the source into a spot with a size of 5 $\mu$m FWHM at the BDA. The BDA can be closed vertically to a size as small as 4 $\mu$m to provide coherent illumination for nanofocusing optics with acceptance up to 350 $\mu$m, such as the upstream optic of a K–B mirror system. The size of the BDA can be opened in both vertical and horizontal directions to utilize partially coherent beam, which allows operation at increased flux, at a cost of reduced spatial resolution.

## III. X-RAY SOURCE

The ISN beamline will use hard X-rays with photon energies from 4 to 30 keV from an insertion device. To access elemental absorption edges of interest, the incident photon energy has to be fully tunable throughout the full range of photon energies. The APS currently operates with a coupling of 1.5 pct and an emittance of 2.514 nm-rad in the horizontal direction. For insertion devices, we use the following standard source parameters (standard lattice "nux36nuy39," courtesy R. Dejus, APS):

$\sigma_x = 274.3\ \mu$m,
$\sigma_y = 10.3\ \mu$m,
$\sigma'_x = 11.27\ \mu$rad,
$\sigma'_y = 3.58\ \mu$rad.

As a reference for the beamline design, we use a number of $s_v = 2.35 \cdot \sigma_y = 24.4\ \mu$m FWHM for the vertical source size.

For the Advanced Photon Source (APS), an insertion device with a period $\lambda_u$ of 3.3 cm provides high brilliance in the first undulator harmonic for energies up to 12 keV, as well as full tunability throughout the range of operating energies. The coherent flux $F_{coh}$, becomes rapidly smaller toward higher energy, with $F_{coh} \sim \lambda^2 \cdot B$, where $\lambda$ is the X-ray wavelength and $B$ the brilliance. We will therefore deploy a "revolver"-type undulator,[38] a device that combines two different periodic structures into a single system, and allows change of the undulator period during experiments. The insertion device for the ISN beamline will utilize a magnetic structure with period $\lambda_u$ of 3.3 cm for the lower part of the energy range, a magnetic structure with period $\lambda_u$ of 2.7 cm for the higher part of energy range, and use the 3rd harmonic of the 3.3 cm structure for the "gap" in the 2.7 cm structure between 15 and 22 keV. Figure 2 shows the tuning curves for both the 3.3 cm structure and the 2.7 cm structure in the relevant energy range, for an electron beam current of 100 mA.

## IV. *IN SITU* NANOPROBE BEAMLINE LAYOUT

The optical concept for the ISN beamline, as discussed in Section I, has to fit into the standard length of APS beamlines of 80 m. The first position that can be used to place beamline optics is directly downstream of the front-end exit window (FEEW), at 25 m from the source. The beamline is laid out to maximize the lateral coherence length at the position of the ISN instrument, thereby maximizing the working distance and space for *in situ* cells. This goal is achieved by positioning the BDA as close to the FEEW as possible, while providing space for slits, mirror systems, and monochromators upstream of the BDA. The beamline optics must be designed to accommodate two canted undulator beams with an angular separation of 1 mrad, corresponding to a spatial separation of 25 mm at the position of the FEEW. Figures 3 and 4 show the layout of the ISN beamline, with the First optical enclosure (FOE) housing the beamline optics for both the ISN beamline and the partner program, and two downstream enclosures housing the Transmission X-ray Microscope (TXM) operated at the second branch beamline, and the ISN instrument, respectively.

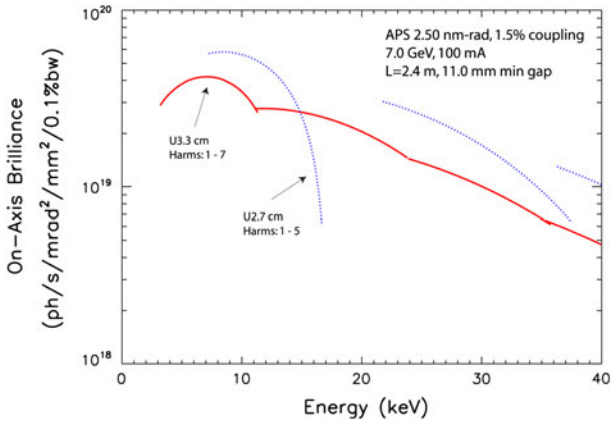


Fig. 2—Brilliance of a revolver-type insertion device. The ISN beamline requires a large-period structure (*e.g.*, 3.3 or 3.0 cm) for continuous tuning through the 4 to 30 keV range, and a smaller-period structure (*e.g.*, 2.7 cm) for higher brilliance at the 7- to 15-keV and 22- to 30-keV energy regimes. The graph shows the brilliance for a 2.4-m-long device (courtesy R. Dejus).

Figure 3 shows the configuration of the major beamline optics in the (FOE). The first optical component, a horizontally deflecting plane mirror, M1, is positioned at 29.7 m from the source, at a grazing angle of 2.5 mrad. It serves as low-pass filter and power filter by rejecting higher undulator harmonic radiation, using reflective stripes of silicon, chromium, and platinum. M1 provides an angular separation between the two canted branch lines of 5 mrad. A vertically deflecting, vertically focusing mirror, M2, is positioned at 35.3 m from the source. It forms a demagnified image of the synchrotron source on the BDA, with a FWHM vertical size of 5.2 $\mu$m. Two additional mirrors located at 31.5 and 33.4 m, respectively are deflecting X-rays from a second insertion device into the second branch beamline. Beam position monitors (BPMs) for the ISN beamline and a pink-beam slit (PBS) are positioned at 36 m. The space between 36.5 m and 38 m is kept free to provide access to the APS ratchet wall doors. A double crystal monochromator (DCM) using Si⟨111⟩ crystals is used to select the photon energy and provide a bandwidth $\Delta E/E = 10^{-4}$, which matches the monochromaticity requirements of diffractive optics with a resolution limit of 20 nm. The DCM is positioned at 38.4 m from the

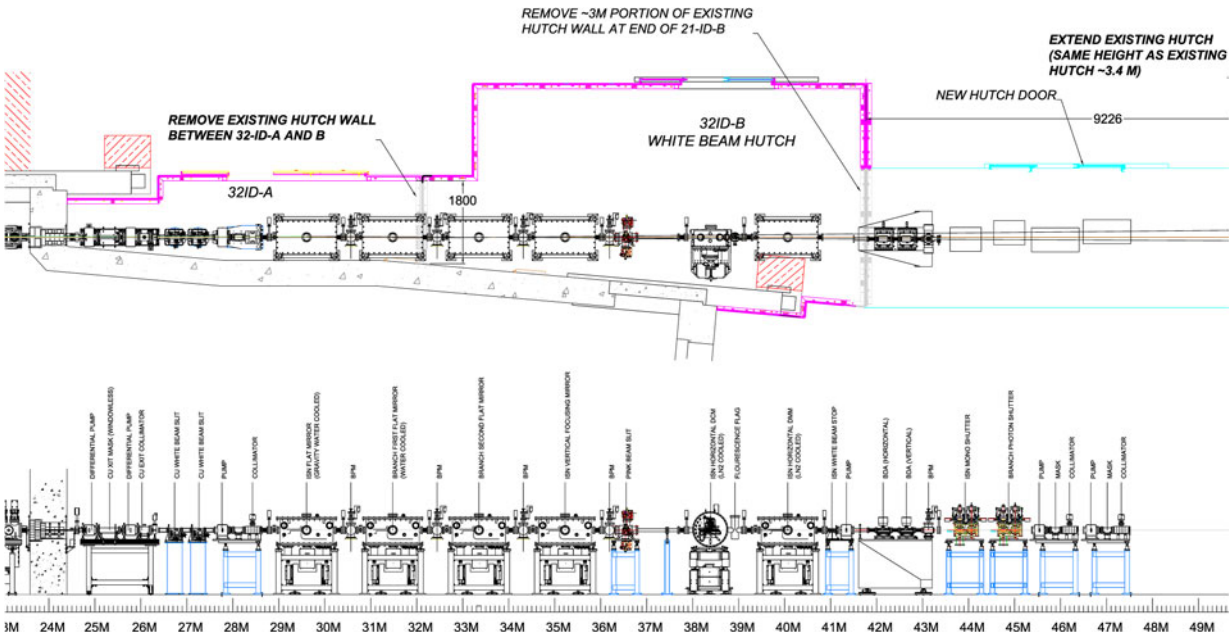


Fig. 3—Layout of the first optical enclosure (FOE). The FOE contains optics for the ISN branch beamline and the TXM branch beamline. Mirror optics for the ISN beamline are positioned at 29.7 and 35.3 m. Mirror optics for the TXM beamline are positioned at 31.5 and 33.4 m. The mirrors provide an angular separation of the two canted beamlines of 14 mrad, leading to a lateral separation of the two undulator beams of 165 mm at 44.5 m from the source.

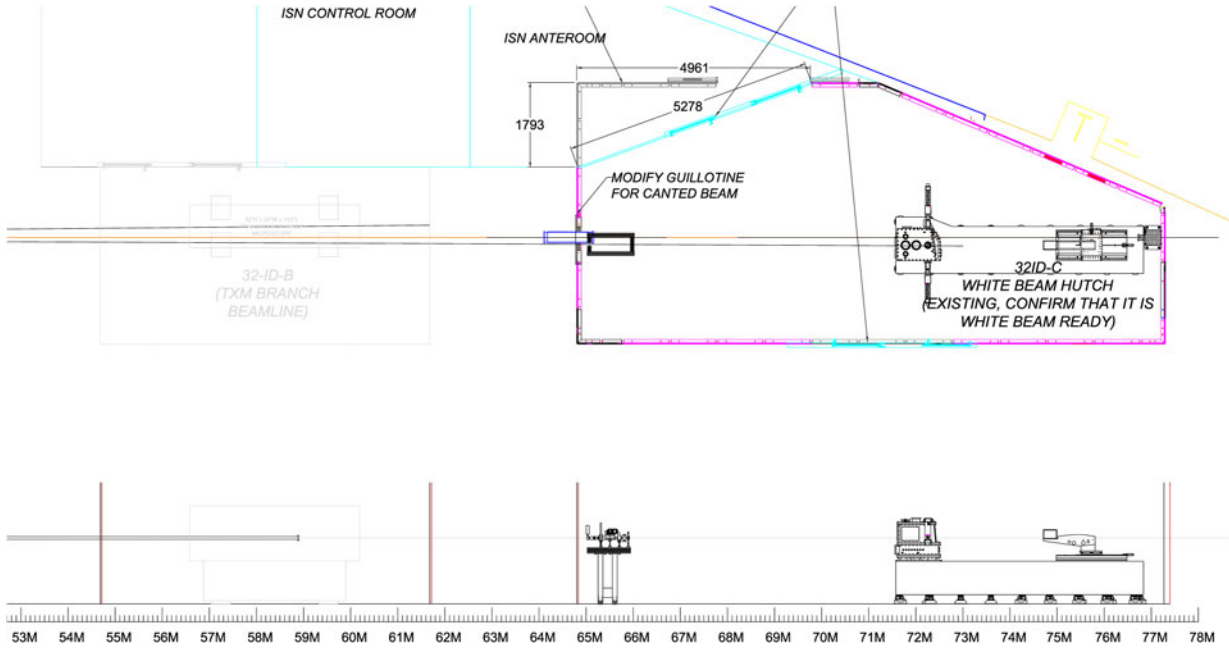


Fig. 4—Layout of the ISN end station and control room. The ISN control room is located on the outboard side of the sector, adjacent to the ISN enclosure, and separated from the enclosure by an anteroom that provides temperature stability and prevents direct air exchange between the control room and the ISN enclosure. The ISN enclosure will be temperature-stabilized to 0.1 °C, and designed to minimize acoustic noise.

source. For operation at 50 nm and above, a double multilayer monochromator (DMM) with $WSi_2/Si$ multilayers will be used for energy selection. It provides a bandwidth of $\Delta E/E = 10^{-2}$, thus exploiting the full intrinsic bandwidth of an insertion devices for highest flux operation. The DMM is positioned at 40.1 m from the source. The BDA is positioned at 42.2 m. For diffraction limited imaging, it will be closed to a size of 11 $\mu$m × 11 $\mu$m for operation with diffractive optics, or to a size of 11 $\mu$m × 4 $\mu$m for operation with KB nanofocusing optics. The DCM for the TXM branch is placed at 44.9 m, where the lateral separation between canted beams is 165 mm. To allow monitoring of the beam position, a BPM is placed after each beamline mirror. For the same purpose, each monochromator is followed by a fluorescence flag.

Slits are required to confine the undulator beam and to regulate total power to various X-ray optical components. The white-beam slit (WBS) for the ISN branch is placed upstream of M1 at 26.7 m; the PBS is placed upstream of the DCM and DMM at 36.5 m. BPMs are placed downstream of each major optical component to allow effective alignment. A removable white-beam monitor, typically a diamond screen, is placed downstream of each mirror at 30.5 and 36.2 m, respectively. A removable fluorescence flag is placed downstream of each monochromator, at 38.8 and 40.8 m.

Figure 4 shows the ISN endstation, where the ISN instrument and related detectors and instrument controls electronics are located. Spatially coherent, monochromatic beam will propagate from the DCM or DMM downstream onto an exit window assembly (EWA) positioned at 65 m. The EWA contains a fast shutter, an absorber setup and a mono-beam slit followed by a small $Si_3N_4$ vacuum window. The fast shutter will be triggered by the data acquisition system, and minimize unnecessary exposure of the sample to ionizing radiation. It will furthermore serve as shutter for a pixel array detector (PAD) used for coherent diffraction imaging. The absorber will be used to limit photon flux to the sample in cases where X-ray beam intensity or detected signal is too high, but the beamline configuration must be maintained out of consideration issues such as beam stability. A mono beam slit (MBS) will be used to match the size of the incident beam to the acceptance of the nanofocusing optics, and thereby minimize the amount of background radiation the sample is exposed to, and effects such as scattering or secondary fluorescence. Beam pipes pumped to a rough vacuum will carry X-rays from the EWA to the ISN instrument chamber.

The ISN instrument will be placed at a position of 72 m from the source. To enable a spatial resolution of 20 nm or below, the enclosure will be temperature-stabilized to 0.1 °C. To prevent temperature fluctuation during access to the instrument, a temperature-stabilized controls room will be constructed. In addition, a small anteroom will be placed between the control room and the entrance to the ISN enclosure. The anteroom serves as an airlock between the control room and the ISN enclosure, and further reduces airflow and temperature instabilities. Further measures for local temperature stabilization, such as small enclosures to temperature-stabilize critical instrument components, will be implemented. To minimize vibrations, the temperature stabilization system will be designed to provide laminar flow to minimize acoustically coupled vibrations. The ISN instrument will be placed on a support structure that is connected to the floor with passively damped supports. The nanofocusing X-ray optics and the sample

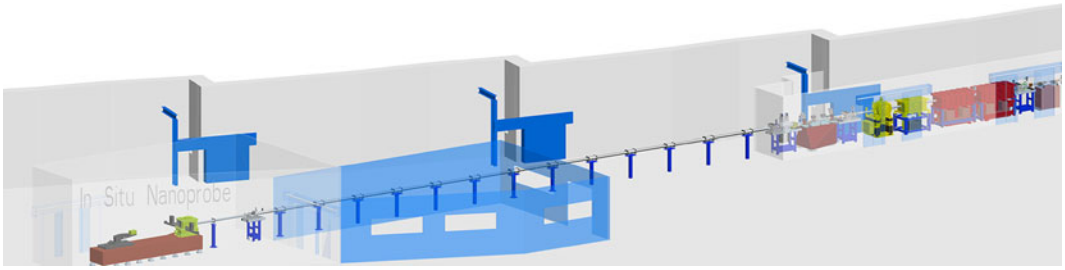


Fig. 5—Overall layout of the *In Situ* Nanoprobe beamline at the Advanced Photon Source. Shown is the ISN configuration, with mirrors (drawn in red), monochromators (drawn in yellow), and the beam defining aperture (drawn in burgundy) positioned in the first optical enclosure, and the ISN instrument in the ISN endstation. The first optical enclosure will contain additional beamline optics for the partner program at the second canted branchline. The ISN enclosure is located in a part of the APS experimental hall were the floor vibrations have small amplitudes. Floor vibrations at the location of the ISN enclosure have been measured to have vertical amplitudes of less than 10 nm RMS in the 1 to 30 Hz band. In addition, the vibrations in all directions are generally lower than vibration criteria curve G (VC-G), which we use as reference.[39] A narrow-band disturbance at 30 Hz is above these levels. This disturbance is caused by experimental hall air handling units located on the APS mezzanine. They will be mitigated before construction of the ISN beamline.

**Table II. Parameters of Diffractive Optics with a Smallest Structure Size of 15 nm**

| Energy Range of operation (keV) | 4 to 6 | 6 to 9 | 8 to 12 | 12 to 18 | 18 to 30 |
|---|---|---|---|---|---|
| Reference Energy (keV) | 5 | 8 | 10 | 15 | 24 |
| Diameter ($\mu$m) | 350 | 235 | 176 | 118 | 74 |
| Number of Zones | 5833 | 3921 | 2941 | 1960 | 1225 |
| Focal Length (mm) | 21.18 | 21.35 | 21.35 | 21.35 | 21.35 |
| Anticipated Type of Optic | ZP | ZP | ZP | ZP/MLL | ZP/MLL |
| Numerical Aperture at reference energy (mrad) | 8.3 | 5.5 | 4.1 | 2.75 | 1.65 |
| Diffraction-Limited Resolution (nm) | 18.3 | 18.3 | 18.3 | 18.3/13.2 | 18.3/13.2 |
| Theoretical Efficiency for Two Stacked Zone Plates with Total Thickness 500 nm (Pct) | 19 to 15 | 15 to 8 | 10 to 4 | 4 to 2 | 2 to 1 |
| Anticipated Efficiency for 2D Focusing MLLs (Pct) | | | | 15 | 20 to 40 |

will be monitored with laser interferometer encoders, and active vibration controls using the encoder readback implemented. Figure 5 shows the overall layout of the ISN beamline.

## V. NANOFOCUSING OPTICS

The ISN instruments will use both diffractive and reflective optics to focus incident hard X-rays into a small probe. Diffractive optics such as ZPs or MLLs will serve as highest-resolution optics, and will be used to focus monochromatic X-rays with a bandwidth of $\Delta E/E = 10^{-4}$ to a focal spot with a size of 20 nm. Reflective optics in Kirkpatrick–Baez (K–B) or Montel geometry will serve as achromatic high-flux optics, and will be used to focus monochromatic X-rays with a bandwidth of up to $10^{-2}$ into a focal spot with a size of 50 nm.

To achieve a diffraction-limited resolution of 20 nm, diffractive optics with smallest structures sizes of 15 nm must be used. At the same time, to achieve good focusing efficiency, diffractive optics have to be fabricated with a thickness corresponding to the interaction length of X-rays with the ZP material, typically in the range of sub-micrometer to several micrometers. ZPs with the required outermost zone width of 15 nm are expected to provide good focusing efficiency in the energy range below 8 to 10 keV; recent developments, based on ZP stacking[40,41] and advanced fabrication methods based on zone-doubling[31] and new materials, might make achieving reasonable efficiency above 10 keV appear possible. MLLs with the required small structures are expected to provide good focusing efficiency in the energy range of 15 keV and above,[42] but require added degrees of freedom for alignment, as compared to ZPs. Development of both technologies will inform the final decision on which high-resolution optics will be deployed in the ISN instrument. Table II lists relevant parameters for ZPs and MLLs. The acceptance of the optics for the respective energy range has been chosen to allow diffraction-limited focusing with the values of the size $d$ of the BDA listed above.

To achieve diffraction-limited focusing with diffractive optics, the zone number $N$ has to be well below the inverse bandwidth of the illuminating beam. For the bandwidth of a Si $\langle 111 \rangle$ monochromator with $\Delta E/E$ of $1.4 \times 10^{-4}$ (at 10 keV), this requires ZPs to have less than 6000 zones. For the parameters listed in Table II, this is well satisfied for photon energies of above 6 keV. The condition can also be satisfied for the energy range of 4 to 6 keV by requiring a ZP diameter $D$ of not more than 350 $\mu$m, at a small loss of coherent photon flux. To obtain a baseline for the focusing efficiency of ZPs, we assume (i) that two ZPs with an outermost zone width of 15 nm and a thickness of 250 nm can be fabricated, (ii) that two such ZPs can be stacked within the optical nearfield, for a total effective thickness of 500 nm. Table II lists the theoretical efficiency of such double-stacked ZPs. Stacking

**Table III. Parameters of Nanofocusing Mirrors**

| Useful Length of Mirror | Physical Length of Mirror | Focal Length | Slope Errors Across Useful Length (rms) | Numerical Aperture (mrad) |
|---|---|---|---|---|
| 60 mm (h) | 70 mm (h) | 60 mm (h) | 0.10 $\mu$rad | 1.25 |
| 170 mm (v) | 175 mm (v) | 180 mm (v) | 0.035 $\mu$rad | 1.25 |

The numerical aperture is calculated for a grazing angle of 2.5 mrad and corresponding acceptance of the mirrors system.

**Table IV. Focused Flux and Flux Density as a Function of Photon Energy, for Operation with Zone Plates and K–B Nanofocusing Mirror System**

| Photon Energy (keV) | 4 | 6 | 8 | 10 | 15 | 20 | 30 |
|---|---|---|---|---|---|---|---|
| Source Brilliance (Photons/s/mm/mrad/ 0.1 pct BW) | $3.94{\cdot}10^{19}$ | $4.89{\cdot}10^{19}$ | $6.97{\cdot}10^{19}$ | $6.84{\cdot}10^{19}$ | $3.35{\cdot}10^{19}$ | $2.53{\cdot}10^{19}$ | $2.26{\cdot}10^{19}$ |
| Zone Plate Efficiency (Pct) | 19 | 15 | 9 | 7 | 3 | 2 | 1 |
| Focusing with Zone Plates, $\sigma$ = 20 nm, $\Delta E/E = 10^{-4}$ | | | | | | | |
| Focused Flux (Photons/s) | $1.80{\cdot}10^{10}$ | $7.83{\cdot}10^{9}$ | $3.77{\cdot}10^{9}$ | $1.84{\cdot}10^{9}$ | $1.72{\cdot}10^{8}$ | $4.85{\cdot}10^{7}$ | $9.64{\cdot}10^{6}$ |
| Flux Density on Sample (Photons/s/$\mu$m$^2$) | $4.50{\cdot}10^{13}$ | $1.96{\cdot}10^{13}$ | $9.41{\cdot}10^{12}$ | $4.60{\cdot}10^{12}$ | $4.29{\cdot}10^{11}$ | $1.21{\cdot}10^{11}$ | $2.41{\cdot}10^{10}$ |
| Focusing with KB Mirrors, $\sigma$ = 50 nm, $\Delta E/E = 10^{-2}$ | | | | | | | |
| Focused Flux, (Photons/s) | $4.54{\cdot}10^{12}$ | $2.51{\cdot}10^{12}$ | $2.01{\cdot}10^{12}$ | $1.26{\cdot}10^{12}$ | $2.75{\cdot}10^{11}$ | $1.16{\cdot}10^{11}$ | $4.63{\cdot}10^{10}$ |
| Flux Density on Sample (Photons/s/$\mu$m$^2$) | $1.82{\cdot}10^{15}$ | $1.00{\cdot}10^{15}$ | $8.03{\cdot}10^{14}$ | $5.05{\cdot}10^{14}$ | $1.10{\cdot}10^{14}$ | $4.66{\cdot}10^{13}$ | $1.85{\cdot}10^{13}$ |

Focused flux for operation with MLLs can be estimated by replacing the efficiency assumed for zone plates with an efficiency for 2D focusing MLLs (Table II).

multiple ZPs without near-field constraint offers in principle an avenue to further increase the focusing efficiency at high energies.[43] For ease of comparison with reflective nanofocusing optics, the numerical aperture NA is listed, with $\mathrm{NA}(E) = 0.5 \times D/f(E)$, where $f$ is the focal length and $E$ the photon energy in the middle of the relevant energy range of operation. The spatial resolution for optics with circular pupil function, such as ZPs, is obtained from $\delta = 0.61 \times \lambda/\mathrm{NA}$. The diffraction limit of optics with rectangular pupil function, such as MLLs and K–B mirror systems, is obtained from $\delta = 0.44 \times \lambda/\mathrm{NA}$.[44]

The focusing performance of K–B mirror system in diffraction limited operation depends on (i) the accuracy of curvature (ii) the numerical aperture of the two mirrors, and (iii) the size of slope errors. Since a K–B system consists of two consecutive curved mirrors, the upstream mirror must have a larger length than the downstream one to provide the same numerical aperture. We have selected parameters that allow the K–B system to accept the full coherent beam at a photon energy of 10 keV. The parameters for the downstream mirror were selected to provide a focal length of 60 mm, corresponding to a working distance of approximately 27 mm. To provide the required numerical aperture, the downstream mirror must have a physical length of 60 mm, and slope errors must be 0.1 $\mu$rad rms or less. To provide the same numerical aperture, the upstream mirror must have a length of 180 mm, a focal length of 175 mm, and slope errors of 0.035 $\mu$rad rms or less. To provide coherent illumination of the long upstream mirror, the BDA must be closed to a vertical size of 4 $\mu$m, as discussed above. Table III summarizes the main parameters of the nanofocusing K–B system for the ISN beamline, as well as the numerical aperture the K–B system provides. The length and slope error specifications for the downstream mirror are well within the current state of the art. The requirements for the upstream mirror are at the edge of what is currently feasible, with 0.05 $\mu$rad rms slope errors over a 350 mm long mirror recently demonstrated.[45]

The ISN will provide a unique combination of very high-focused flux at a spot size of 50 nm, highest spatial resolution of 20 nm or below using diffractive optics and coherent diffraction, and trace element sensitivity down to the level of 50 to 150 atoms for most metals. Table IV lists the focused flux and flux density on the sample, as estimated for the ISN instrument; Table V lists the minimum detection limit for both operation with a ZP using a DCM, and for operation with the K–B mirror system using a DMM. For nanospectroscopic experiments at 50 nm resolution, a DCM will be used in conjunction with the K–B mirror system, leading to 100 times improved energy resolution, at cost of a 25 times reduction in focused flux compared to operation with a DMM. For the purpose of this estimate, a reflectivity of 80 pct was assumed for the mirror system for the full spectral range of the beamline.

In Table V, the elemental sensitivity of the ISN for both a low-Z metal (Zn) with binding energy close to 10 keV, and an intermediate-Z metal (Ru) with binding energy close to 25 keV are listed. The sensitivity is based on fluorescence and scattering background measured at the 2-ID-D microprobe at APS, and thus provides a realistic estimate of the actual sensitivity that can be expected.

## VI. *IN SITU* NANOPROBE INSTRUMENT

The ISN instrument is located at 72 m from the source. It will be supported on a vibration-isolated

Table V. Minimum Detection Limit (MDL) for the ISN Beamline

| Minimum Detection Limit, for Dwell Time of 1 Second | # of Zn Atoms $E = 10$ keV | # of Ru Atoms $E = 25$ keV |
|---|---|---|
| Elemental Mapping, $\delta = 50$ nm, $\Delta E/E = 10^{-2}$ | 60 | 90 |
| Elemental Mapping, $\delta = 20$ nm, $\Delta E/E = 10^{-4}$ | 90 | 150 |
| Nano-XANES, $\delta = 50$ nm, $\Delta E/E = 10^{-4}$ | 560 | 930 |

The MDL values for Zn and Ru are based on spectra measured with incident photon energies of 10 and 22.2 keV, respectively, at the 2-ID-D beamline, and include actual background. A dwell time of 1 second is assumed.

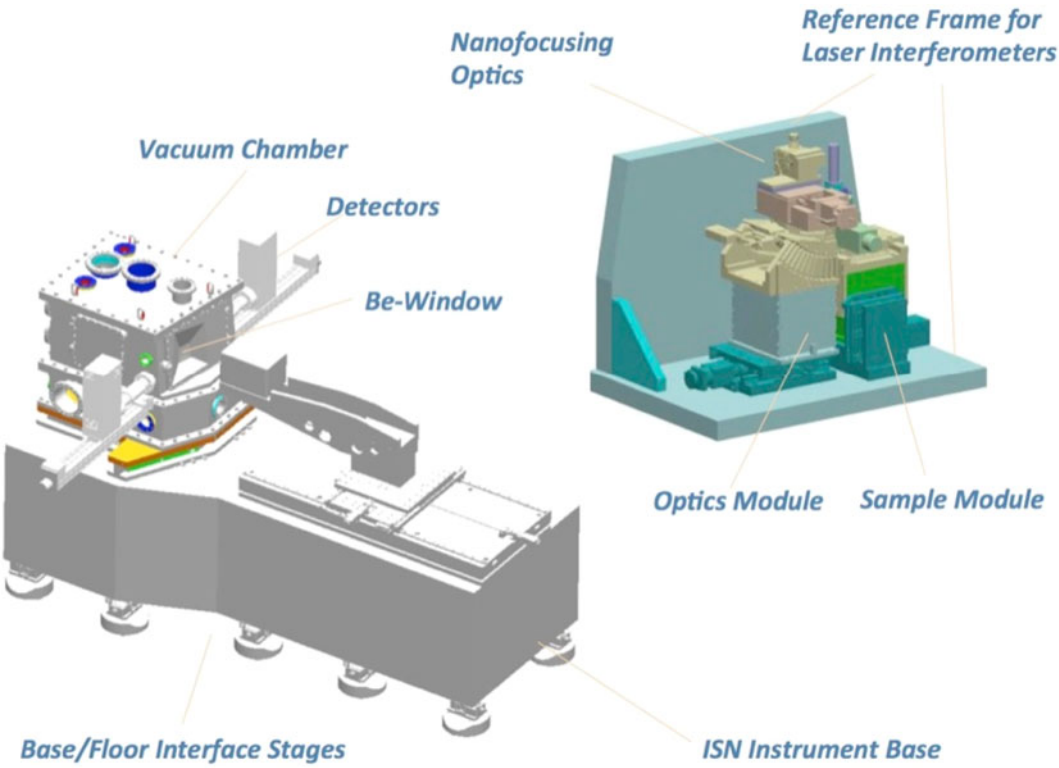


Fig. 6—Conceptual design of the *In Situ* Nanoprobe instrument. The insert shows a design for the nanopositioning unit and laser-based encoders. The nanopositioning mechanics carry both a nanofocusing mirror and several Fresnel zone plate.

structure to minimize coupling of floor vibration into the instrument. The sample, optics, and nanopositioners will be housed in an instrument chamber, to allow operation in a vacuum or under inert gases.

At the core of the ISN instrument is the nanopositioning unit, which consists of an optics module, a sample module and a reference platform, which carries optics and sample modules, as well as a multi-axis laser interferometer. The reference platform is made of Invar, to minimize thermally induced drifts of positioners and encoders. The laser interferometer serves as encoder and provides real-time positioning information on optics and specimens. Laser interferometer fiber optics heads are mounted on the reference platform. Reflectors are positioned on the optics module and the specimen module, in close proximity to the X-ray optics and sample, respectively. The reference platform will be mounted inside the ISN instrument chamber at three points, in a fashion that decouples it from changes of the instrument chamber due to pressure or temperature variation. The instrument chamber also includes a mechanism for specimen change, energy-dispersive detectors, prealignment optics, viewports, and other auxiliary components. X-rays enter the instrument chamber through a $Si_3N_4$ window on the upstream side. A larger window will be mounted on the downstream side to allow propagation of the transmitted wavefront to a PAD downstream of the instrument. This allows use of coherent diffraction techniques in small-angle geometry. The PAD is mounted on a slide that moves parallel to the X-ray axis, allowing the distance between the PAD and sample to change as a function of desired scattering angle and photon energy. Figure 6 shows the layout of the ISN instrument.

To study materials and devices under *in situ* conditions, environmental specimen cells are required. These cells must be consistent with highly accurate positioning, must allow exchange of gases and fluids, must provide connections for application of external fields, and must provide heating and cooling capability. We will develop cartridge-based specimen cells that connect to an interface plate with proper connections for electrical leads,

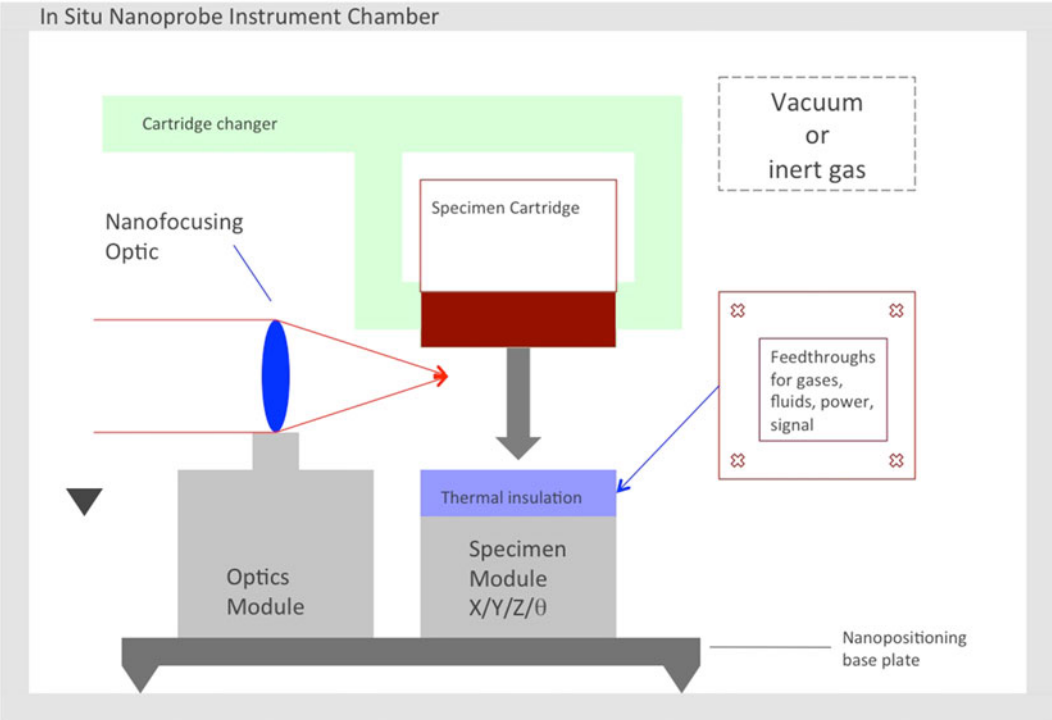


Fig. 7—Concept for *in situ* specimen cartridge. The cartridge-system is designed to allow use of a multitude of optimized environment. The cartridge system consists of the actual specimen environment and a mating, temperature-insulating interface plate that is mount that is stiffly to the specimen module. The interface plate that will be connected to external sources of gases, fluids, and coolants, and provide connectors for electrical power and sensor channels. The specimen cartridge will connect to the interface plate and the various feedthroughs. The cartridges will provide internal heating capability and temperature sensors. The environmental cartridges will contain X-ray windows to isolate the internal environment, as well as protect the X-ray optics positioned upstream of the sample stage. A mechanical cartridge changer will allow transfer of the specimen cartridge from outside the instrument chamber onto the specimen module.

gases, and fluids. The cartridges will be suitable for adaptation to each of the specific environmental parameters, or combinations thereof, as outlined above. For example, variable-temperature cartridges for heating to high temperatures of well above 1273 K (1000 °C), as well as for cooling to 40 K (−233 °C) will be developed. Cartridges that allow application of external fields and read-back of electrical currents, combined with flow of gases and/or fluids will also be developed. This approach will allow development of new and customized cartridges for specific experiments that may not have been proposed to date, without requiring significant modification to the ISN instrument. The approach will also allow external user groups to develop their own cartridges, and bring them to experiments. Figure 7 shows a concept for environmental cartridges suitable for a wide variety of specific *in situ* and *operando* experiments.

## VII. EXAMPLE OF SCIENTIFIC APPLICATION: INORGANIC PHOTOVOLTAIC DEVICES

The vast majority of solar cells (photovoltaic devices) are comprised of semiconductors, a class of materials that is sensitive to trace impurity concentrations.[46,47] Over the past decade, synchrotron-based techniques have been extensively applied to multicrystalline silicon (mc-Si), a material that now comprises the absorber layer of 54 pct of all panels shipped to customers in 2012. Synchrotron investigations played a large role in the technological development of this material system, as outlined in the next paragraph. As newer materials, with lower-cost, higher yield, higher efficiency or otherwise more desirable properties, such as lower weight or less rigidity, are now being explored as candidate replacements for multicrystalline silicon, advanced synchrotron techniques are vital to better understand the properties of these materials under various fabrication and operation conditions. Building on existing capabilities, it is essential to exploit higher measurement throughput, improved sensitivity and *in situ* measurement capabilities to more fully understand the materials systems and make rapid progress toward deployable next-generation devices.

The technological evolution of mc-Si was greatly influenced by industry-academia partnerships involving synchrotron measurements, especially $\mu$-XRF and $\mu$-XAS. The developments detailed forthwith highlight the contributions of synchrotron investigations, which occurred within the context of a vigorous worldwide scientific community engaged in laboratory-based studies. During the late 1990s, the first $\mu$-XRF investigations into mc-Si were reported, revealing that fast-diffusing metal impurities present at recombination-active extended defects[48,49] can be manipulated during thermal

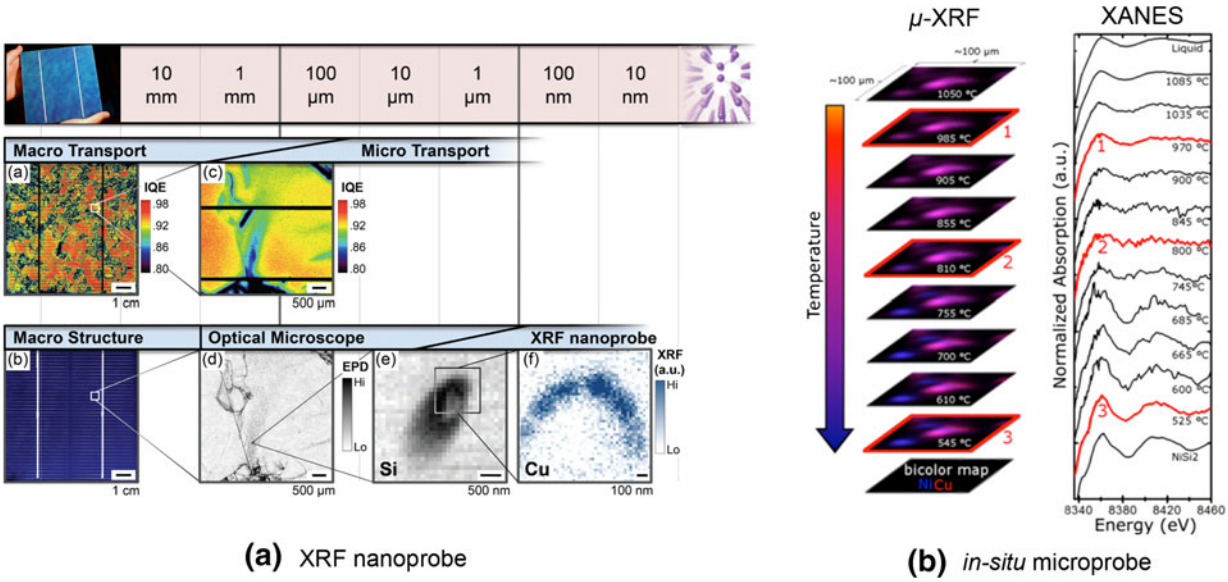


Fig. 8—(*a*) Device impacts and (*b*) evolution of metal-impurity/structural-defect interactions in silicon-based solar cell materials, explored by (a) nanoprobe beamline (APS 26-ID-C) and (b) *in situ* microprobe characterization with $\mu$-XRF in slew scan mode and Quick-XAS (ALS 10.3.2). The proposed beamline envisions combining high-throughput scanning, *in situ*, operando, high sensitivity, and high-spatial resolution capabilities. Figures (a) and (b) from Refs. [66] and [67], respectively.

treatments.[50] During the 2000s, bulk metal-impurity concentrations in commercial mc-Si were revealed to be orders of magnitude higher than expected,[51] with the vast majority of metals contained in second-phase nanoprecipitates in weakly bonded metal-silicide chemical states.[52–54] Realizing that metal impurities could be intentionally engineered to improve the quality of even heavily contaminated mc-Si materials[55,56] a plethora of novel manufacturing processes appeared in the 2010s and were widely disseminated in industry,[57–60] resulting in efficiency and yield enhancements.[61] In summary, sustained synchrotron investigations into "wild-type" commercial multicrystalline silicon and "model systems" yielded such a high degree of microstructural insight, that predictive engineering of certain performance-limiting defects is now possible. Additionally, synchrotron investigations helped to reveal the natures of certain types of electrical shunts,[62] reverse-bias breakdown mechanisms,[63] crucible contamination sources,[64] and defect interactions,[65] helping improve module performance and reliability.

These insights were fueled by a parallel effort to expand the range and capabilities of synchrotron-based measurement techniques. The X-ray beam-induced current (XBIC) technique was developed to study the electrical impact of defects while simultaneously collecting $\mu$-XRF/XAS data, by measuring the X-ray photogenerated carrier collection efficiency.[68,69] A more elegant, contactless method relying on X-ray excited optical luminescence was later developed.[70,71] *In situ* high-temperature $\mu$-XRF/XAS measurements, and $\mu$-XRF measurements with sub-100 nm spatial resolution yielded unprecedented insights into defect behavior and interactions, as shown in Figure 8 (Reference10).

Today, researchers are exploring new classes of photovoltaic materials with fundamentally lower cost structures and higher performance than today's mc-Si. These materials include the chalcogenides copper zinc tin sulfide (CZTS, Reference 72) and copper indium gallium diselenide (CIGS, References 73 and 74), which benefit from lower materials usage and more streamlined manufacturing processes than mc-Si. However, microscopic bulk defects limit industrial device performance. The quaternary nature of these phases adds complexity and increases the potential for defects involving lattice constituents (*e.g.*, phase decomposition). To study these effects in a statistically meaningful manner, fast compositional $\mu$-XRF/XAS measurements are required. To illustrate the envisioned high-throughput scanning and data acquisition capabilities of the ISN, Figure 9 compares current state-of-the-art $\mu$-XRF mapping at APS Beamline 2-ID-D against the designed throughput of the ISN. Because of the superior fluorescence count rates of the ISN and integrated slew scan capability, the ISN will achieve throughput improvements on the order of two orders of magnitude and beyond with far superior sensitivity, compared to state-of-the-art beamlines and instruments. For samples with heterogeneities on various length scales, high-throughput mapping is essential to yield statistically meaningful microstructural insights.

For understanding issues such as defect kinetics, chemical interactions between contaminant species and correlation between microstructure and electronic properties, *in situ* and *operando* measurements are essential. The ISN is designed to measure samples under realistic processing conditions at variable temperatures, while controlling the gas ambient to prevent oxidation. *Operando* electrical performance measurements can simultaneously be acquired. ISN beamline-compatible sample mounts are being developed for such experiments in a collaboration involving ASU, MIT, and the

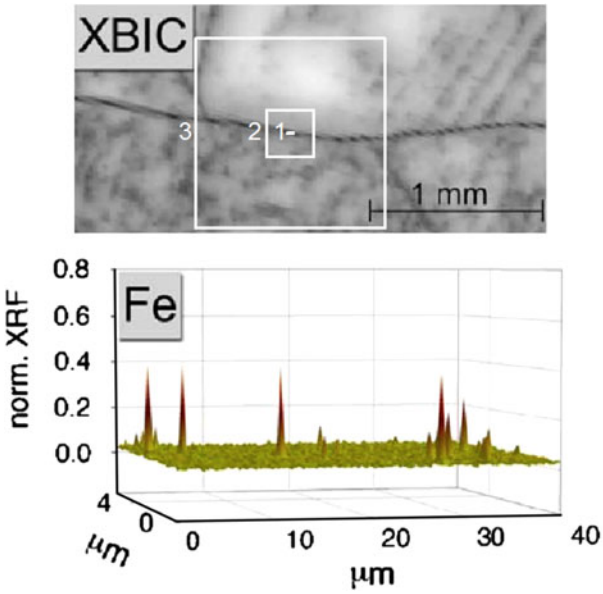


Fig. 9—Impact of high-throughput $\mu$-XRF measurements for the study of complex, hierarchical materials. In the upper figure (marked "XBIC"), the recombination activity of a mc-Si silicon grain boundary is mapped at low resolution using the XBIC technique. A region along the grain boundary is selected for $\mu$-XRF mapping to probe for metal precipitates. The actual size of a $\mu$-XRF map obtained at APS Beamline 2-ID-D is marked "1" on the XBIC map and is shown below (Fe), detecting approximately a dozen Fe-rich precipitates. This $\mu$-XRF measurement of 160 $\mu m^2$ required 2 hours of acquisition time (1500 ms per point (ms/pt), 200 nm per pixel). With higher $\mu$-XRF measurement throughput of the ISN, 2 hours of acquisition time could yield scan areas of $5 \times 10^4$ $\mu m^2$ (marked "2" on the XBIC map; assumes 0.25 ms/pt, 50 nm/pixel) and $1 \times 10^6$ $\mu m^2$ (marked "3"; assumes 0.25 ms/pt, 200 nm/pixel), with 50 to 100 times magnification increased elemental sensitivity. Experimental data from Ref. [75].

APS; these sample mounts should also be useful for studying a variety of other energy materials and systems under realistic processing and operating conditions. The aforementioned non-destructive *in situ* and *operando* capabilities of the ISN distinguish it from other closely related techniques, including atom probe tomography and transmission electron microscopy.

## VIII. SUMMARY

The ISN beamline is a next-generation hard X-ray nanoprobe beamline designed for *in situ* and *operando* studies of materials and devices, with particular emphasis on energy related systems, such as photovoltaic systems, advanced batteries, and fuel cell components, as well to explore approaches for sustainable energy, such as carbon sequester and advanced building materials. The ISN will be installed as a new flagship beamline at a canted undulator beamline at the Advanced Photon Source. The ISN will deploy a K–B mirror system to focus X-rays to a spot size of 50 nm for high-throughput X-ray florescence spectroscopy and X-ray fluorescence tomography, and use diffractive optics for focusing to 20 nm for the highest resolution studies. The instrument will provide an elemental sensitivity of approximately 100 atoms for most elements in the periodic system. The ISN will use coherent diffraction techniques in small-angle transmission geometry in parallel to acquiring X-ray fluorescence data, allowing to study structural sample features at sub-10 nm resolution in parallel to acquisition of distribution and chemical state of trace elements. Using a cartridge-based approach, the instrument will deploy a variety of *in situ* environments, including a heating/cooling stage with a temperature range of 40 K (233 °C) to 773 K (500 °C), a high-temperature stage capable of reaching temperatures above 1273 K (1000 °C), and several stages that combine flow of fluids and gases with applied electrical fields and currents.

## ACKNOWLEDGMENTS

We thank Wenjun Liu for continued productive discussions on nanofocusing mirrors and nanopositioning. We thank Oliver Schmidt for his help in beamline design work, Roger Dejus for preparing tuning curves for the ISN undulator, and Lahsen Assoufid for his suggestions on X-ray mirrors. We furthermore thank our colleagues Seth Darling, Conal Murray, Tijana Rajh, Wilson Chiu, Ken Kemner, Paolo Monteiro, Ellery Ingall, Yong Chu, and Hanfei Yan for their valuable scientific and technical discussions, and their continued engagement in the ISN facility. T.B. acknowledges funding from U.S. Department of Energy SunShot Initiative under Contracts No. DE-EE0005314, DE-EE0005329, and DE-EE0005948. Use of the Advanced Photon Source (APS) at Argonne National Laboratory was supported by the US Department of Energy, Office of Science, Office of Basic Energy Sciences, under Contract No. DE-AC02-06CH11357.

## REFERENCES

1. J.M. Maser, R.P. Winarski, M. Holt, D. Shu, C. Benson, B. Tieman, C. Preissner, A. Smolyanitskiy, B. Lai, S. Vogt, G. Wiemerslage, and G.B. Stephenson: *Proc. 8th Int. Conf. X-ray Microsc., IPAP Conf. Ser.* 2006. Vol. 7, pp. 26–29.
2. S. Chen, C. Flachenecker, B. Lai, T. Paunesku, B. Hornberger, C. Roehrig, J. VonOsinski, M. Bolbat, J. Maser, D. Shu, L. Finney, S. Gleber, Q. Jin, K. Brister, C. Jacobsen, S. Vogt, and G. Woloschak: *Microsc. Microanal.*, 2012, vol. 18, pp. 962–63.
3. R.P. Winarski, M.V. Holt, V. Rose, P. Fuesz, D. Carbaugh, C. Benson, D. Shu, D. Kline, G.B. Stephenson, I. McNulty J. Maser: *J. Synchrotron Rad.*, 2013, vol. 19 (6), pp. 1056–60.
4. C.G. Schroer, P. Boye, J.M. Feldkamp, J. Patommela, D. Samberg, A. Schropp, A. Schwab, S. Stephan, G. Falkenberg G. Wellenreuther, and N. Reimers: *Nucl. Instrum. Methods Phys. Res. A*, 2010, vol. 616, p. 93.
5. P. Bleuet, P. Cloetens, P. Gergaud, D. Mariolle, N. Chevalier R. Tucoulou, J. Susini, and A. Chabli: *Rev. Sci. Instrum.*, 2009, vol. 80, p. 056101.
6. A. Somogyi, C.M. Kewish, F. Polack, and T. Moreno: *AIP Conf. Proc.*, 2011, vol. 1365, pp. 57–60.
7. Y.S. Chu: in *Preliminary Design Report for the Hard X-ray (HXN) Nanoprobe Beamline. National Synchrotron Light Source II, Brookhaven National Laboratory, LT-C-XFD-HXN-PDR-001*, 2010.

8. D. Oosterhout, M.M. Wienk, S.S. van Bavel, R. Thiedmann, L.J.A. Koster, J. Gilot, J. Loos, V. Schmidt, and R.A.J. Janssen: *Nature Mater*., 2009, vol. 8, p. 818.
9. S. Hudelson, B.K. Newman, S. Bernardis, D.P. Fenning, M.I. Bertoni, M.A. Marcus, S.C. Fakra, B. Lai, and T. Buonassisi: *Adv. Mater*., 2010, vol. 22, pp. 3948–53.
10. M.I. Bertoni, D.P. Fenning, M. Rinio, V. Rose, M. Holt, J. Maser, and T. Buonassisi: *Energy Environ. Sci*., 2011, vol. 4, pp. 4252–57.
11. S.B. Darling: *Energy Environ. Sci*., 2009, vol. 2, p. 1266.
12. M. Nikiforov, B. Lai, W. Chen, S. Chen, R.D. Schaller, J. Strzalka, J. Maser, and S.B. Darling: *Energy Environ. Sci*., 2013, vol. 6, pp. 1513–20. DOI:10.1039/c3ee40556g.
13. A. Faes, A. Hessler-Wyser, D. Presvytes, C.G. Vayenas J. Van Herle: *Fuel Cells*, 2009, vol. 9 (6), pp. 841–51.
14. P. Tanasini, M. Cannarozzo, P. Costamagna, A. Faes, J. Van Herle, A. Hessler-Wyser, and C. Comninellis: *Fuel Cells*, 2009, vol. 9, pp. 740–52.
15. K.N. Grew, Y.S. Chu, J. Yi, A.A. Peracchio, J.R. Izzo, Jr, Y. Hwu, F. De Carlo, and W.K.S. Chiua: *J. Electrochem. Soc*., 2010, vol. 157, pp. B783–92.
16. C.J. Kiely, J. Fink, M. Brust, D. Bethel, and D.J. Schiffrin: *Nature*, 1998, vol. 396, p. 444.
17. H. Xiong, M. Slater, M.D. Balasubramanian, C.S. Johnson, and T. Rajh: *J. Phys. Chem. Lett*., 2011, vol. 2, pp. 2560–65.
18. H. Xiong, H. Yildirim, E.V. Shevchenko, V.B. Prakapenka, B. Koo, M.D. Slater, M. Balasubramanian, S.K.R.S. Sankaranarayanan, J.P. Greeley, S. Tepavcevic, N.M. Dimitrijevic, P. Podsiadlo C.S. Johnson, and T. Rajh: *J. Phys. Chem. C*, 2012, vol. 116, pp. 3181–87.
19. Z. Tokei, K. Croes, and G. Beyer: *Microelectron. Eng*., 2010, vol. 87, p. 348.
20. C. Lavoie, C. Detavernier, C. Cabral, Jr, F. d'Heurle, A. Kellock, J. Jordan-Sweet, and J.M.E. Harper: *Microelectron. Eng*., 2006, vol. 83, p. 2042.
21. D. Mangelinck, K. Hoummada, O. Cojocaru-Miredin, E. Cadel, C. Perrin-Pellegrino, and D. Blavette: *Microelectron. Eng*., 2008, vol. 85, p. 1995.
22. J. Schaeffer, D.C. Gilmer, C. Capasso, S. Kalput, B. Taylor, M. Raymond, D. Triyoso, R. Hedge, S. Samavedan, and B. White, Jr: *Microelectron. Eng*., 2007, vol. 84, p. 2196.
23. C.E. Murray, A. Ying, S.M. Polvino, I.C. Noyan, M. Holt J. Maser: *Appl. Phys*., 2011, vol. 109, p. 083543-1.
24. C. Shi, P.V. Krivenko, and D.M. Roy: *Alkali-Activated Cements and Concretes*, Taylor & Francis, Abingdon, 2006, p. 376.
25. J.L. Provis, V. Rose, S.A. Bernal, and J.S.J. van Deventer: *Langmuir*, 2009, vol. 25, p. 11897.
26. J. Eun Oh, P.J.M. Monteiro, S.S. Jun, S. Choi, and S.M. Clark: *Cem. Concr. Res*., 2010, vol. 40 (2), pp. 189–96.
27. C.R. Benitez-Nelson: *Earth Sci. Rev*., 2000, vol. 51, pp. 109–35.
28. L.B. Skinner, S.R. Chae, C.J. Benmore, H.R. Wenk, and P. Monteiro: *Phys. Rev. Lett*., 2010, vol. 104(19), 195502.
29. S.B. Baines, B.S. Twining, S. Vogt, W.M. Balch, N.S. Fisher, and D.M. Nelson: *Deep Sea Res. II*, 2010, vol. 58, pp. 512–23.
30. J.L. Provis, V. Rose, R.P. Winarski, and J.S.J. van Deventer: *Scripta Mater*., 2011, vol. 65, p. 316.
31. J. Vila-Comamala, Y. Pan, J. Lombardo, W.M. Harris, W.K. Chiu, C. David, and Y. Wang: *J. Synchrotron Rad*., 2012, vol. 19, pp. 705–09.
32. J. Vila-Comamala, S. Gorelick, E. Färm, C.M. Kewish, A. Diaz, R. Barrett, V.A. Guzenko, M. Ritala, and C. David: *Opt. Express*, 2011, vol. 19, pp. 175–84.
33. H. Yan, V. Rose, D. Shu, E. Lima, H.C. Kang, R. Conley, C. Liu, N. Jahedi, A.T. Macrander, G.B. Stephenson, M.V. Holt, Y.S. Chu, M. Lu, and J. Maser: *Opt. Express*, 2011, vol. 19, pp. 15069–76.
34. H. Mimura, S. Handa, T. Kimura, H. Yumoto, D. Yamakawa, H. Yokoyama, S. Matsuyama, K. Inagaki, K. Yamamura, Y. Sano, K. Tamasaku, Y. Nishino, M. Yabashi, T. Ishikawa, and K. Yamauchi: *Nat. Phys*., 2009, vol. 6, pp. 122–25.
35. W. Liu, G.E. Ice, L. Assoufid, C. Liu, B. Shi, R. Khachatryan, J. Qian, P. Zschack, J.Z. Tischler, and J.-Y. Choi: *J. Synchrotron Rad*., 2011, vol. 18, pp. 575–79.
36. I. Peterson, B. Abbey, C.T. Putkunz, D.J. Vine, G.A. van Riessen, G.A. Cadenazzi, E. Balaur, R. Ryan, H.M. Quiney, I. McNulty, A.G. Peele, and K.A. Nugent: *Opt. Express*, 2012, vol. 20, pp. 24678–85.
37. D.J. Vine, D. Pelliccia, C. Holzner, S.B. Baines, A. Berry I. McNulty, S. Vogt, A.G. Peele, and K.A. Nugent: *Opt. Express*, 2012, vol. 20, pp. 18287–96.
38. B. Stillwell, J.H. Grimmer, D. Pasholk, and E. Trakhtenberg: *Proc. Int. Part. Accel. Conf. IPAC 2012*. New Orleans, LA. 2012. p. 750.
39. H. Amick, M. Gendreau, T. Busch, and C. Gordon: *Buildings for Nanoscale Research and Beyond*, SPIE, San Diego, CA, 2005, pp. 1–13.
40. J. Maser, B. Lai, W. Yun, S.D. Shastri, Z. Cai, W. Rodrigues, S. Xu, and E. Trakhtenberg: in *Proc. SPIE*., vol. 4783, D.C. Mancini, ed., 2002, pp. 74–81.
41. S.D. Shastri, J.M. Maser, B. Lai, and J. Tys: *Opt. Commun*., 2001, vol. 197, pp. 1–3.
42. H. Chol Kang, H. Yan, R.P. Winarski, M.V. Holt, J. Maser, C. Liu, R. Conley, S. Vogt, A.T. Macrander, and G.B. Stephenson: *Appl. Phys. Lett*., 2008, vol. 92, p. 221114.
43. J. Vila-Comamala, M. Wojcik, A. Diaz, M. Guizar-Sicairos, C.M. Kewish, S. Wang, and C. David: *J. Synchrotron Rad*., 2013, vol. 20, pp. 434–40. DOI:10.1107/S090904951300263X.
44. W. Liu: *Rev. Sci. Inst*., 2005, vol. 76, p. 113701.
45. F. Siewert, J. Buchheim, S. Boutet, G.J. Williams, P.A. Montanez, J. Krzywinski, and R. Signorato: *Opt. Express*, 2012, vol. 20, pp. 4525–36.
46. G. Coletti, P.C.P. Bronsveld, G. Hahn, W. Warta, D. Macdonald, B. Ceccaroli, K. Wambach, N.L. Quang, and J.M. Fernandez: *Adv. Funct. Mater*., 2011, vol. 21, pp. 879–90.
47. R. Rocheleau, S. Hegedus, W. Buchanan, and R. Tullman: *Proc. 19th IEEE Photovolt. Specialists Conf*. 1987, pp. 699–704.
48. S.A. McHugo, A.C. Thompson, I. Périchaud, and S. Martinuzzi: *Appl. Phys. Lett*., 1998, vol. 72, pp. 3482–84.
49. O.F. Vyvenko, T. Buonassisi, A.A. Istratov, E.R. Weber M. Kittler, and W. Seifert: *J. Phys. Condens. Matter*, 2002, vol. 14, pp. 13079–86.
50. S.A. McHugo: *Appl. Phys. Lett*., 1997, vol. 71, pp. 1984–86.
51. A.A. Istratov, T. Buonassisi, R.J. McDonald, A.R. Smith R. Schindler, J.A. Rand, J.P. Kalejs, and E.R. Weber: *J. Appl. Phys*., 2003, vol. 94, pp. 6552–59.
52. T. Buonassisi, A.A. Istratov, M. Heuer, M.A. Marcus, R. Jonczyk, J. Isenberg, B. Lai, Z. Cai, S.M. Heald, W. Warta R. Schindler, G. Willeke, and E.R. Weber: *J. Appl. Phys*., 2005, vol. 97, p. 074901.
53. M. Heuer, T. Buonassisi, A.A. Istratov, M.D. Pickett, M.A. Marcus, A.M. Minor, and E.R. Weber: *J. Appl. Phys*., 2007, vol. 101, p. 123510.
54. T. Buonassisi, M. Heuer, A.A. Istratov, M.D. Pickett, M.A. Marcus, B. Lai, Z. Cai, S.M. Heald, and E.R. Weber: *Acta Mater*., 2007, vol. 55, pp. 6119–26.
55. T. Buonassisi, A.A. Istratov, M.A. Marcus, B. Lai, Z. Cai, S.M. Heald, and E.R. Weber: *Nat. Mater*., 2005, vol. 4, pp. 676–79.
56. T. Buonassisi, A.A. Istratov, M.D. Pickett, M. Heuer, J.P. Kalejs, G. Hahn, M.A. Marcus, B. Lai, Z. Cai, S.M. Heald, T.F. Ciszek, R.F. Clark, D.W. Cunningham, A.M. Gabor, R. Jonczyk, S. Narayanan, E. Sauar, and E.R. Weber: *Prog. Photovolt. Res. Appl*., 2006, vol. 14, pp. 513–31.
57. J. Schön, H. Habenich, M.C. Schubert, and W. Warta: *J. Appl. Phys*., 2011, vol. 109, p. 063717.
58. J. Hofstetter, D.P. Fenning, M.I. Bertoni, J.F. Lelièvre, C. del Cañizo, and T. Buonassisi: *Prog. Photovolt*., 2011, vol. 19, pp. 487–97.
59. D. Macdonald, S.P. Phang, F.E. Rougieux, S.Y. Lim, D. Paterson, D.L. Howard, M.D. de Jonge, and C.G. Ryan: *Semicond. Sci. Technol*., 2012, vol. 27, p. 125016.
60. D.P. Fenning, J. Hofstetter, M.I. Bertoni, G. Coletti, B. Lai, C. del Cañizo, and T. Buonassisi: *J. Appl. Phys*., 2013, vol. 113, p. 044521.
61. D.M. Powell, D.P. Fenning, J. Hofstetter, J.F. Lelièvre, C. del Cañizo, and T. Buonassisi: *Proc. 37th IEEE Photovoltaic Specialists Conference*, Seattle, WA, 2011.
62. T. Buonassisi, O.F. Vyvenko, A.A. Istratov, E.R. Weber, G. Hahn, D. Sontag, J.P. Rakotoniaina, O. Breitenstein, J. Isenberg, and R. Schindler: *J. Appl. Phys*., 2004, vol. 95, pp. 1556–61.
63. W. Kwapil, P. Gundel, M.C. Schubert, F.D. Heinz, W. Warta, E.R. Weber, A. Goetzberger, and G. Martinez-Criado: *Appl. Phys. Lett*., 2009, vol. 95, p. 232113.

64. T. Buonassisi, A.A. Istratov, M.D. Pickett, J.-P. Rakotoniaina, O. Breitenstein, M.A. Marcus, S.M. Heald, and E.R. Weber: *J. Cryst. Growth*, 2006, vol. 287, pp. 402–07.
65. T. Buonassisi, A.A. Istratov, M.D. Pickett, M.A. Marcus, T.F. Ciszek, and E.R. Weber: *Appl. Phys. Lett.*, 2006, vol. 89, p. 042102.
66. M.I. Bertoni, D.P. Fenning, M. Rinio, V. Rose, M. Holt, J. Maser, and T. Buonassisi: *Energy Environ. Sci.*, 2011, vol. 4, pp. 4252–57.
67. S. Hudelson, B.K Newman, S. Bernardis, D.P. Fenning, M.I. Bertoni, M.A. Marcus, S.C. Fakra, B. Lai, and T. Buonassisi: *Adv. Mater.*, 2010, vol. 22, pp. 3948–53.
68. O.F. Vyvenko, T. Buonassisi, A.A. Istratov, H. Hieslmair, A.C. Thompson, R. Schindler, and E.R. Weber: *J. Appl. Phys.*, 2002, vol. 91, pp. 3614–17.
69. T. Buonassisi, A.A. Istratov, M.D. Pickett, M.A. Marcus, G. Hahn, S. Riepe, J. Isenberg, W. Warta, G. Willeke, T.F. Ciszek, and E.R. Weber: *Appl. Phys. Lett.*, 2005, vol. 87, p. 044101.
70. P. Gundel, G. Martinez-Criado, M.C. Schubert, J.A. Sans, W. Kwapil, W. Warta, and E.R. Weber: *Phys. Status Solidi RRL*, 2009, vol. 3, pp. 275–77.
71. O. Vyvenko, T. Arguirov, W. Seifert, I. Zizak, M. Trushin, and M. Kittler: *Phys. Status Solidi A*, 2010, vol. 207, pp. 1940–43.
72. D.B. Mitzi, O. Gunawan, T.K. Todorov, K. Wang, and S. Guha: *Sol. Energy Mater. Sol. Cells*, 2011, vol. 95, p. 1421.
73. A. Chirila, S. Buecheler, F. Pianezzi, P. Bloesch, C. Gretener, A.R. Uhl, C. Fella, L. Kranz, J. Perrenoud, S. Seyrling, R. Verma, S. Nishiwaki, Y.E. Romanyuk, G. Bilger, and A.N. Tiwari: *Nat. Mater.*, 2011, vol. 10, pp. 857–61.
74. M.A. Contreras, L.M. Mansfield, B. Egaas, J. Li, M. Romero, R. Noufi, E. Rudiger-Voigt, and W. Mannstadt: *Prog. Photovolt.*, 2012, vol. 20, pp. 843–50.
75. T. Buonassisi, A.A. Istratov, S. Peters, C. Ballif, J. Isenberg, S. Riepe, W. Warta, R. Schindler, G. Willeke, Z. Cai, B. Lai, and E.R. Weber: *Appl. Phys. Lett.*, 2005, vol. 87, p. 121918.